



# Quaternion Grassmann average network for learning representation of histopathological image

Jun Shi<sup>a</sup>, Xiao Zheng<sup>a</sup>, Jinjie Wu<sup>a</sup>, Bangming Gong<sup>a</sup>, Qi Zhang<sup>a</sup>, Shihui Ying<sup>b,\*</sup>

<sup>a</sup>Institute of Biomedical Engineering, School of Communication and Information Engineering, Shanghai University, 200444 Shanghai, China

<sup>b</sup>Department of Mathematics, School of Science, Shanghai University, 200444 Shanghai, China

## ARTICLE INFO

### Article history:

Received 2 September 2017

Revised 7 November 2018

Accepted 15 December 2018

Available online 19 December 2018

### Keywords:

Principal component analysis network

(PCANet)

Quaternion algebra

Quaternion Grassmann averages network

(QGNet)

Color histopathological image

## ABSTRACT

Histopathological image analysis works as 'gold standard' for cancer diagnosis. Its computer-aided approach has attracted considerable attention in the field of digital pathology, which highly depends on the feature representation for histopathological images. The principal component analysis network (PCANet) is a novel unsupervised deep learning framework that has shown its effectiveness for feature representation learning. However, PCA is susceptible to noise and outliers to affect the performance of PCANet. The Grassmann average (GA) is superior to PCA on robustness. In this work, a GA network (GANet) algorithm is proposed by embedding GA algorithm into the PCANet framework. Moreover, since quaternion algebra is an excellent tool to represent color images, a quaternion-based GANet (QGNet) algorithm is further developed to learn effective feature representations containing color information for histopathological images. The experimental results based on three histopathological image datasets indicate that the proposed QGNet achieves the best performance on the classification of color histopathological images among all the compared algorithms.

© 2018 Elsevier Ltd. All rights reserved.

## 1. Introduction

Cancers seriously threaten human health, and therefore it is always highly demanded for the most accurate diagnosis of cancers. It is well known that the high-resolution histopathological image is a 'gold standard' for the diagnosis of almost all types of cancer in clinical practice [1,2]. However, this kind of pathology diagnosis is highly dependent on the subjective decisions of pathologists [2,3]. Therefore, it is necessary to develop a computer-aided diagnosis (CAD) or quantitative analysis system for histopathological image analysis, which can help the pathologists reduce the workload, and more importantly, the possibility of errors, as a second opinion tool [1–7]. Moreover, it also can provide an effective decision support tool for the training of young radiologists [1–7].

In a CAD system, feature representation is one of the most critical steps. For example, the commonly used features in histopathological images mainly represent the local cell-level information (e.g., size and shape) or the holistic architecture of tissue (e.g., topology and layout of all cells) [1,5]. For more details on the hand-crafted features based histopathological image classification, we refer to [1,3,5,8–10]. Although a remarkable progress of various feature extraction methods has been achieved, the hand-

crafted features mostly have poor generalization ability among the histopathological images of different cancers [11,12]. Therefore, feature representation has become a fairly decisive factor in histopathological image based CAD, while it is still very challenging [12].

In the past several years, deep learning (DL) has demonstrated superior performance to the hand-crafted features in various applications [13–15]. It has also gained a good reputation in the feature representation of histopathological images [6,7,12]. Cireşan et al. first used convolutional neural networks (CNN) to detect mitosis in breast histopathological images and won the mitosis detection competition in ICPR 2012 contest [16]. Then, various CNN-based DL algorithms have been developed for the purpose of cell detection and counting, cell segmentation and tissue classification for histopathological images [3,17–32]. Except for the CNN framework, other DL algorithms, including the stacked auto-encoder (SAE), restricted Boltzmann machine (RBM), deep belief networks (DBN) and their variants, have also been successfully applied to histopathological images, especially for cell detection [8,33–37]. All these DL-based methods show superior or even state-of-the-art performance for histopathological images.

More recently, Chan et al. proposed a principal component analysis network (PCANet) algorithm [38]. PCANet is essentially an unsupervised DL framework, which only has three simple basic components: the cascaded PCA as a deep network, binary hashing as

\* Corresponding author.

E-mail address: [shying@shu.edu.cn](mailto:shying@shu.edu.cn) (S. Ying).

a nonlinear layer, and block-wise histograms for feature pooling layer. PCANet has shown its effectiveness for feature representation learning. Moreover, compared with the commonly used DL algorithms, PCANet has the advantages of simpler network architecture and fewer parameters. Therefore, PCANet and its variants, such as DLANet [39], SRDANet [40], SPCANet [41], 2DPCANet [42], MPCANet [43], and R-VCANet [44], have been widely used for various image classification tasks.

The effectiveness of PCANet for image representation makes it feasible for histopathological image analysis. Moreover, since PCANet is an unsupervised learning algorithm, it is more suitable for medical image processing in the small dataset case. On the other hand, in histopathological images, the noises and outliers are inevitable, and they can result from artifact, non-standardized staining protocol, focusing inaccuracy, diversity of imaging devices, diversity of resolution, etc. [1,9]. Therefore, some small regions in a histopathological image may be affected by noise and outliers. PCA is sensitive to noise and outliers, resulting in the degeneration of robustness [45], and then further affects the ability of the feature representation in PCANet. Therefore, it is critical to improve the robustness of the PCA in the PACNet framework. Fortunately, Grassmann averages (GA) can address this issue by averaging all subspaces generated by the data on the Grassmann manifold to realize dimensionality reduction [46]. It is worth noting that GA is consistent with PCA in the Gaussian data case, while it is more robust than PCA [46]. The experimental results have shown that GA outperforms PCA on several tasks in computer vision, such as dimensionality reduction, background modeling, image restoration and shadow removal [46]. Since histopathological images always carry noise and outliers during the imaging procedure, GA algorithm would have superior performance over PCA for the dimensionality reduction of histopathological images. Moreover, inspired by the PCANet framework, we will construct a GA based network (GANet) with the similar network framework in this work.

Hematoxylin and Eosin (H&E) staining is commonly used to reveal cellular components and enhance the visibility of spatial structures of histological components in clinical practice, which makes the color information particularly important and helpful for diagnosis. As a result, many color descriptors have been widely used to represent histopathological images [1,2]. However, the existing GA algorithm can only handle grayscale images. When a color histopathological image is converted into the grayscale one, rich color information will be lost, which leads to deteriorated feature representation. Although we can conduct the GANet algorithm on each color channel image and then concatenate them to form the fused color features, the intrinsic correlation among the color channels is discarded by this color information fusion strategy [1]. Therefore, it is essential to integrate color information into GANet such that more effective representation of histopathological images can be learned.

Quaternion algebra was first proposed by Hamilton in 1866 [48]. It has been demonstrated that quaternion algebra is excellent at color image representation mathematically. It comprises one real and three imaginary parts, and these three imaginary parts are used to represent the three different color channels, respectively. Various quaternion-based feature extraction algorithms for color images have been proposed in recent years [49–53], especially the quaternion PCA (QPCA) [54]. More recently, Zeng et al. proposed the quaternion PCANet that outperforms PCANet for the feature representation of color images [55]. A novel algorithm, named quaternion GA (QGA), is therefore considered by integrating the quaternion algebra and the GA algorithm. We will further develop a novel QGA network (QGANet) algorithm according to the PCANet framework [46].

In this work, we develop a QGANet algorithm that can effectively learn the feature representation of the color histopathologi-

cal images for cancer diagnosis based on our previous work [56]. The main contributions of this work are threefold: (1) A GANet algorithm is first proposed to improve the robustness of the learned representative features for gray histopathological images; (2) The QGA algorithm is then developed by incorporating the quaternion algebra into GA algorithm for the dimensionality reduction of color images; (3) The QGANet algorithm, which can learn more effective feature representations from color histopathological images, is finally proposed.

## 2. Quaternion Grassmann average network

Fig. 1 shows the proposed QGANet, which is composed of four components: the quaternion representation model, the cascaded QGA model, the binary hashing model and the block-wise histograms model.

We take a two-layer cascaded QGA network as an example in this work. It is worth noting that GANet has four components, the same as QGANet, but it only has the cascaded GA filters without the quaternion representation. We will introduce these components in the following sections.

### 2.1. Quaternion Grassmann average algorithm

#### 2.1.1. Quaternion representation for color image

Let  $M_p$  be a color image and  $\{M_p\}_{p=1}^P$  be the set of images. From the quaternion representation,  $M_p$  is described by

$$M_p = U(M_p) + I(M_p)i + J(M_p)j + K(M_p)k \quad (1)$$

where  $U(M_p)=0$ ,  $I(M_p)$ ,  $J(M_p)$  and  $K(M_p)$  are the image components of red, green and blue channels, respectively, in a color image, and  $i$ ,  $j$  and  $k$  are the corresponding imaginary units. Here, the real part of the quaternion is set to zero due to the pure quaternion representation. The imaginary units satisfy the following operator rules

$$\begin{cases} i^2 = j^2 = k^2 = ijk = -1 \\ ij = -ji = k \\ jk = -kj = i \\ ki = -ik = j \\ \|M_p\| = \sqrt{U(M_p)^2 + I(M_p)^2 + J(M_p)^2 + K(M_p)^2} \end{cases} \quad (2)$$

It can be found that quaternion representation holistically integrates different color channels of a pixel by a quaternion number. Therefore, the quaternion algebra theory is then successfully used for color image processing. One of the advantages is that the correlation among different color channels can be effectively exploited in 3D or 4D space conveniently.

#### 2.1.2. Grassmann average

To improve the robustness of feature representation, the Grassmann Average (GA) algorithm has been developed to express dimensionality reduction as an average of the subspaces spanned by the data [46]. GA is inherently more robust than PCA where it overcomes the shortage of PCA for the scale data.

PCA can be regarded as fitting a  $D$ -dimensional ellipsoid to the data, where every axis of the ellipsoid represents a principal component [47]. It can be modeled as following optimization problem to calculate the first weight vector  $v_1$

$$v_1 = \operatorname{argmax}_{\|v\|=1} \|Xv\|^2 = \operatorname{argmax}_{\|v\|=1} \sum_{i=1}^n (x_i^T v)^2, \quad (3)$$

where  $X$  is the centered data matrix and  $x_i$  is the row vector of  $X$ . PCA cannot scale to large datasets due to the SVD solution only fits for the low-dimensional cases [46]. Moreover, PCA can also be regarded as finding the subspace in which the projected data are as similar as possible to the original data.

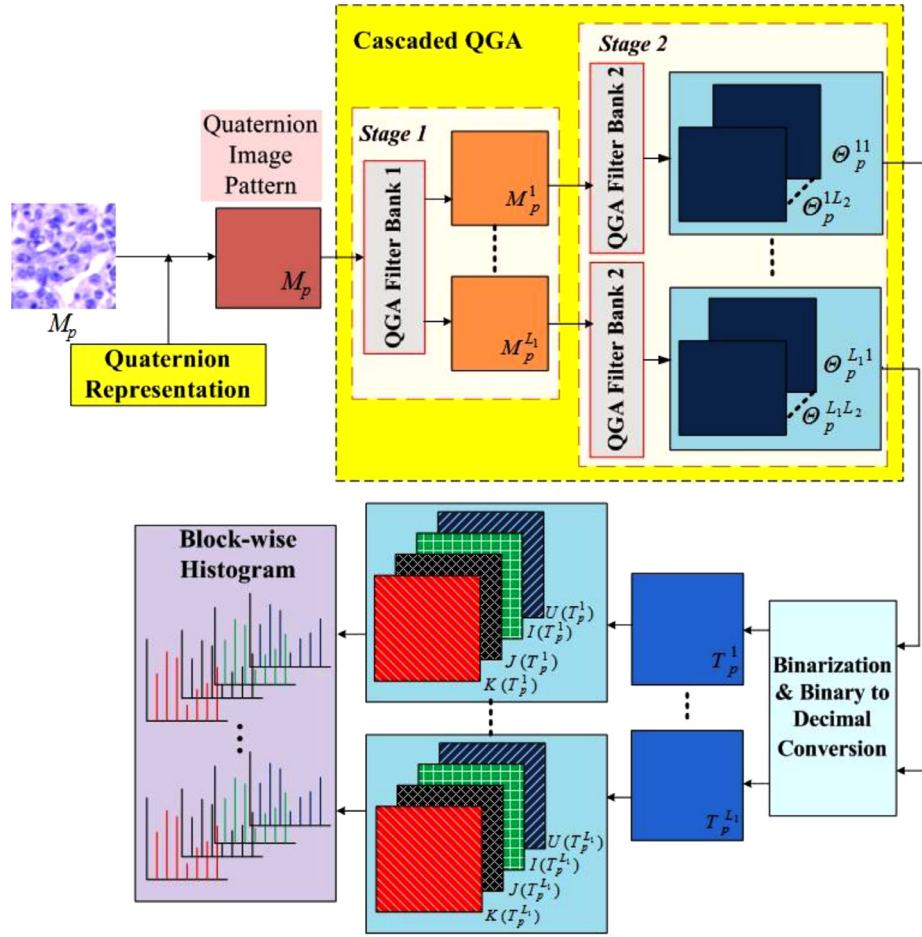


Fig. 1. Flowchart of the QGANet model.

The dimensionality reduction problem can be reconsidered by the average of  $N$  1-dimensional subspace. It should be pointed out that all 1-dimensional subspace forms the Grassmann manifold  $Gr(1, D)$  [46]. A unit vector  $u$  or its antipode  $-u$  can be selected to represent a certain 1-dimensional subspace, which includes  $u$ . That is, all elements in this 1-dimensional subspace are equivalent to these representative elements. Hence,  $Gr(1, D)$  can be written as the quotient space  $S^{D-1}/\{\pm 1\}$  of the unit sphere in  $R^D$  with respect to the equivalent relation  $1 \sim -1$ . Then, for any nonzero vector  $x_n \in R^D$ , we select the representation element of its spanned subspace by

$$[u_n] = x_n / \|x_n\| \quad (4)$$

Then, the Grassmann average subspace is defined by the first principle component (PC). The Grassmann weighted average is defined by minimizing the following weighted sum-of-squared distances

$$[q^*] = \arg \min_{[v] \in Gr(1, D)} \sum_{n=1}^N w_n \text{dist}_{Gr(1, D)}^2([u_n], [v]) \quad (5)$$

For this minimizing problem, there is an efficient algorithm to solve it. Given the properties of averages, the GA is expected to be more robust to outliers than the ordinary PCA for general distributions.

### 2.1.3. Quaternion Grassmann average

The proposed QGA extends the original GA algorithm from the domain of real numbers  $R^D$  to the domain of quaternion numbers  $Q^{\bar{D}}$ , where  $D = 4\bar{D}$ . Let  $\{x_n\}_{n=1}^N$  be a zero-mean color patch

dataset extracted from  $\{M_p\}_{p=1}^P$ . For this color image dataset, the Grassmann manifold  $Gr(k, \bar{D})$  is the set of all  $k$ -dimensional linear subspaces of  $Q^{\bar{D}}$  [46]. For example, each sample, spanning a 1-dimensional subspace of  $Q^{\bar{D}}$ , is a point in the Grassmann manifold  $Gr(1, \bar{D})$ . Then, for any nonzero vector  $x_n \in Q^{\bar{D}}$ , we select the representation element of its spanned subspace by

$$[u_n] = U(u_n) + I(u_n)i + J(u_n)j + K(u_n)k := x_n / \|x_n\| \quad (6)$$

In next step, by substituting Eq. (6) and quaternion representation  $v = U(v) + I(v)i + J(v)j + K(v)k$  into Eq. (5), then which is equivalently rewritten as

$$[q] = \arg \min_{[v] \in Gr(1, \bar{D})} \sum_{n=1}^N w_n \text{dist}_{Gr(1, \bar{D})}^2([u_n], [v]) \quad (7)$$

where  $w_n$  is the weight and  $\text{dist}_{Gr(1, \bar{D})}$  is the geodesic distance on the Grassmann manifold  $Gr(1, \bar{D})$ . This distance is defined by the minimal geodesic distance on the unit sphere  $S^{\bar{D}-1}$ .

$$\text{dist}_{Gr(1, \bar{D})}^2([u_1], [u_2]) = \min\{\text{dist}_{S^{\bar{D}-1}}^2(v_1, v_2) | v_1 \in [u_1], v_2 \in [u_2]\} \quad (8)$$

It can be validated that for any weighted average  $[q] \in Gr(1, \bar{D})$  of  $[u_1], \dots, [u_N]$  and arbitrary  $q \in [q] \subset S^{\bar{D}-1}$ , there exists  $u_i, \dots, u_N \subset [u_i], i = 1, \dots, N$  such that  $q$  is a weighted average on  $S^{\bar{D}-1}$  [46]. That is,

$$q = \arg \min_{v \in S^{\bar{D}-1}} \sum_{n=1}^N w_n \text{dist}_{S^{\bar{D}-1}}^2(u, v) \quad (9)$$

Further, the geodesic distance on the unit sphere  $S^{\bar{D}-1}$  is always defined by

$$\text{dist}_{S^{\bar{D}-1}}^2(u_1, u_2) = \frac{1}{2} \|u_1 - u_2\|^2 = 1 - u_1^T u_2 \quad (10)$$

From Eqs. (8) and (10), we have

$$\text{dist}_{Gr(1, \bar{D})}^2([u_1], [u_2]) = 1 - |u_1^T u_2| \quad (11)$$

and Eq. (7) is then reformulated as

$$q = \arg \max_{v \in S^{\bar{D}-1}} \sum_{n=1}^N |x_n^T v| \quad (12)$$

Under the minimizing problem defined in (9), the weighted average of data  $u_1, \dots, u_N \in S^{\bar{D}-1}$  has the closed form of

$$q = \frac{(\sum_{n=1}^N \omega_n)^{-1} \sum_{n=1}^N \omega_n u_n}{\left\| (\sum_{n=1}^N \omega_n)^{-1} \sum_{n=1}^N \omega_n u_n \right\|} \quad (13)$$

where the weight  $\omega_n$  is always selected as  $\|x_n\|$  for normalization. Then, the QGA subspace can be calculated with an iterative scheme as

$$\begin{aligned} \omega_{n,t} &= \text{sign}(u_n^T [u]_{t-1}^*) \|x_n\| \\ q_t &= \frac{(\sum_{n=1}^N \omega_{n,t})^{-1} \sum_{n=1}^N \omega_{n,t} u_n}{\left\| (\sum_{n=1}^N \omega_{n,t})^{-1} \sum_{n=1}^N \omega_{n,t} u_n \right\|} \end{aligned} \quad (14)$$

where  $[u]_t^* = U(u_t^*) + I(u_t^*)i + J(u_t^*)j + K(u_t^*)k$  is the first PC, and  $t$  is the iteration number. Note that Eq. (14) converges to a local optimum.

Through the above algorithm, the first PC of the data is calculated. All other PCs are then calculated sequentially in a greedy way by adding an orthogonal constraint. The algorithm is executed by removing all estimated principal components from the data and then computing the next component from the residual. Formally, for the data matrix  $X \in Q^{N \times D}$ , the updating  $\hat{X} \leftarrow X - (Xq)q^T$  is executed on the data matrix where the component  $q$  is removed [46]. The next component is then calculated on  $\hat{X}$  in the same way. Thus, all PCs can be successfully obtained for the dimensionality reduction.

## 2.2. QGA Network (QGANet)

### 2.2.1. Cascaded QGA network

For a training image dataset  $\{M_p\}_{p=1}^P$ , an  $h_1 \times h_2$  patch should be extracted around the center pixel, and thus we can obtain the amount of training patches for PCA. Suppose that there are  $L_r$  filters in the  $r$ th-layer. Then, in the first-layer of the QGA network, the  $L_1$  leading components  $q_{l_1}$  ( $l_1 = 1, 2, \dots, L_1$ ) are calculated for each patch by the proposed QGA algorithm. The QGA filters in the first stage are given by

$$W_{l_1}^1 = \text{mat}_{h_1, h_2}(q_{l_1}) \in Q^{h_1 \times h_2}, \quad l_1 = 1, 2, \dots, L_1 \quad (15)$$

where  $\text{mat}_{h_1, h_2}(\cdot)$  is a function that maps  $q \in Q^{h_1 h_2}$  to a matrix  $W \in Q^{h_1 \times h_2}$  by rearranging an  $h_1 h_2$ -dimensional vector as an  $h_1 h_2$  matrix.

Then, the output of the  $l_1$ -th filter in the first stage is given by

$$M_p^{(l_1)} = M_p * W_{(l_1)}^1, \quad p = 1, 2, \dots, P \quad (16)$$

where the symbol  $*$  denotes the 2D quaternion convolution, which is also linear.

Furthermore, we simply construct the next layer of the network in the same way. For example, as the input  $M_p^{l_1}$  for the second

stage,  $L_2$  outputs are generated by convolving  $M_p^{l_1}$  with  $W_{l_2}^2$  such as

$$\Theta_p^{l_2} = \{M_p^{l_1} * W_{l_2}^2\}_{l_2=1}^{L_2}, \quad l_2 = 1, 2, \dots, L_2 \quad (17)$$

We can add more layers to construct the deeper QGA networks with the same way.

### 2.2.2. Binary hashing and block-wise histogram

After the two-level QGA networks are concededly built, we obtained  $L_1 L_2$  quaternion output images in total. Then, we use the following characteristic function to binary quantize four parts of each output quaternion image  $\Theta_p^{l_2}$ .

$$\chi(x) = \begin{cases} 1, & x > 0 \\ 0, & x \leq 0 \end{cases} \quad (18)$$

By regarding the binary pixel values at the same location as a  $L_2$  bits vector, we pull the  $L_2$  outputs back to a new single integer-valued image:

$$\begin{aligned} T_p^{(l_1)} &= \sum_{(l_2=1)}^{(L_2)} 2^{(l_2-1)} \tilde{\Theta}_p^{(l_2)} = U(T_p^{(l_1)}) + I(T_p^{(l_1)})i + J(T_p^{(l_1)})j \\ &\quad + K(T_p^{(l_1)})k, \quad p = 1, 2, \dots, P \end{aligned} \quad (19)$$

By using the inverted quaternion representation process, we decompose the color image into four grayscale images  $T_p^{l_1}$ . As shown in Fig. 1,  $T_p^{l_1}$  can be decomposed into  $U(T_p^{l_1})$ ,  $I(T_p^{l_1})$ ,  $J(T_p^{l_1})$  and  $K(T_p^{l_1})$ , where every pixel is an integer-valued with range of  $[0, 2^{L_2} - 1]$ .

Finally, each of the final images  $T_p^{l_1}$  ( $l_1 = 1, \dots, L_1$ ) is partitioned into  $K$  blocks. The histogram (with  $2^{L_2}$  bins) of the decimal values is then computed in each block, which can be concatenated into one vector as the final output features of QGANet. Since  $T_p^{l_1}$  has four parts, namely,  $U(T_p^{l_1})$ ,  $I(T_p^{l_1})$ ,  $J(T_p^{l_1})$  and  $K(T_p^{l_1})$ , each part can be calculated separately.

## 2.3. QGANet-based classification algorithm

In PCANet, all the block histogram features are concatenated to form the final feature vector. Although it is simple to generate feature representation, the feature vector always has high dimensionality. Furthermore, this feature vector misses the spatial information of images. To address these issues, we then adopt the spatial pyramid pooling (SPP) algorithm in [57] to re-organize the learned local histogram features generated in GANet or QGANet. It should be noted that the SPP effectively protects the image's spatial information and hence it generates more effective mid-level feature representation. On the other hand, the local patches are densely sampled from the binary-to-decimal conversion images, and hence the local histogram features are extracted from these local patches. Therefore, the SPP incorporates the spatial arrangement into image representation by hierarchically pooling these local features, as shown in Fig. 2. More details about the SPP algorithm, please refer to [57].

The features gained from SPP are finally fed to the widely used linear support vector machine (SVM) for the classification of color histopathological images [58]. It should be noted that only  $L_1$  images are generated by the binary-to-decimal conversion in QGANet, and therefore the SPP is conducted on each of these  $L_1$  images. Furthermore, the final output features for SVM are the concatenation of all the  $L_1$  SPP features. Fig. 3 shows the flowchart of QGANet-based classification algorithm for color histopathological images.



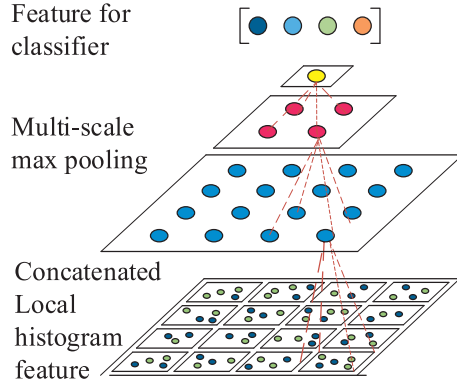


Fig. 2. Flowchart of the spatial pyramid pooling algorithm.

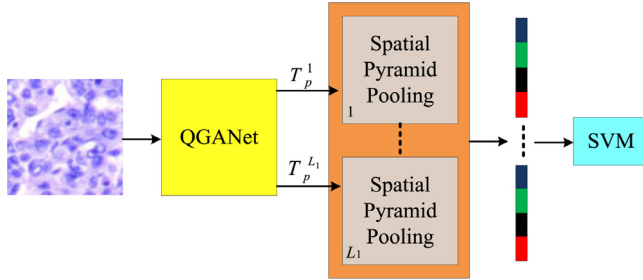


Fig. 3. Flowchart of the QGANet-based classification algorithm for color histopathological images.

### 3. Experiment and results

#### 3.1. Dataset

We then evaluate GANet and QGANet respectively on the following three histopathological image datasets, whose typical example images are shown in Fig. 4.

- (1) Hepatocellular carcinoma (HCC) image dataset [59]. This HCC dataset was acquired by the Olympus BX51 at the Medical College of Nantong University. It includes 66 HCC images in total (21 well differentiated images, 23 moderately differentiated images and 22 poorly differentiated images) [59]. The image size is  $1024 \times 768$  pixels.
- (2) Beth Israel Deaconess Medical Center (BIDMC) breast cancer image dataset [60]. This breast cancer image dataset was approved by the BIDMC IRB, and images were scanned using a Philips Scanner. There are 20 ductal carcinoma in situ (DCIS) images and 31 usual ductal hyperplasia (UDH) images, and each image has the size of  $1444 \times 901$  pixels [60].
- (3) Animal Diagnostics Lab (ADL) kidney image dataset [61]. This ADL dataset was kindly provided by the Animal Diagnostics Lab, Pennsylvania State University [61]. We randomly selected 100 kidney histopathological images (50 inflammatory images and 50 healthy images) with the size of  $1360 \times 1024$  pixels.

#### 3.2. Experimental design

Two experiments were then conducted for GANet and QGANet, respectively. GANet was evaluated on the grayscale histopathological images that were converted from the original color histopathological images, while QGANet was tested on color histopathological images.

GANet was compared with the following algorithms: (1) PCANet [38]; (2) the sparse coding (SC) based classification algorithm with linear spatial pyramid matching [62], which is a kind of classical

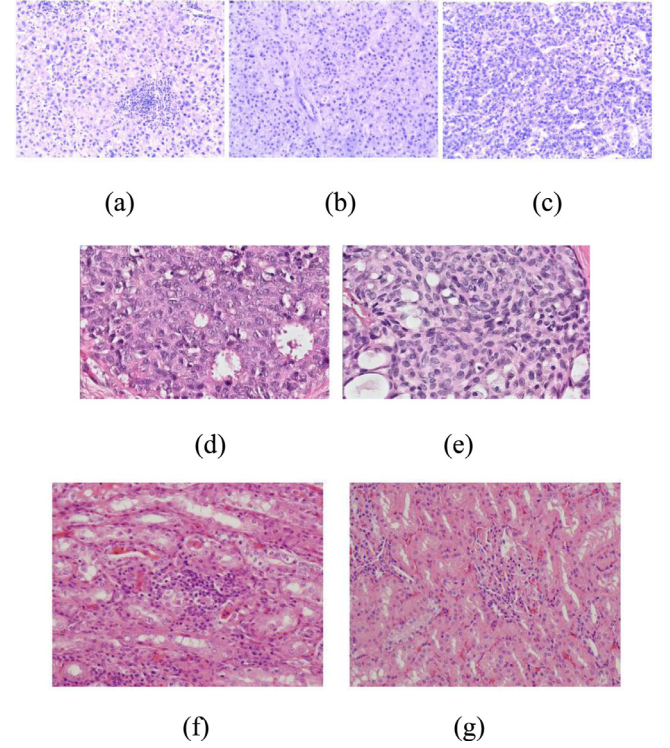


Fig. 4. Example images of three color histopathological image datasets. (a)–(c) are the well differentiated liver image, the moderately differentiated liver image and the poorly differentiated liver image in the HCC dataset, respectively; (d) and (e) are the DCIS image and UDH image in BIDMC dataset, respectively; (f) and (g) are the inflammatory image and the health image in the ADL-Kidney dataset, respectively.

Table 1

Parameters of SAE and DBN for the HCC dataset.

	SAE	DBN
Hidden node	110	130
Layer	3	2 RBMs
Batch size	500	100
Epoch	600	800

Table 2

Parameters of SAE and DBN for the BIDMC dataset.

	SAE	DBN
Hidden node	100	100
Layer	3	2 RBMs
Batch size	500	200
Epoch	500	450

image classification algorithms; (3) DBN [63]; and (4) SAE [64]. Both the SAE and DBN had three-layer network architectures, and their optimal parameters were set through multiple experiments. It is worth noting that the unsupervised DBN and SAE without fine-tuning were selected in our experiment for a fair comparison, since GANet is an unsupervised deep learning algorithm. Tables 1–3 show the parameters of the SAE and DBN for different datasets, which have been fine-tuned to achieve the best performance.

QGANet was then compared with the following algorithms on color images: (1) the joint SC (JSC) algorithm for color histopathological images in [37], which fuses color information by building joint dictionary and learning joint sparse representation; (2) the DBN-based algorithm for color histopathological images (named DBN-RGB), which would first decompose the color images into R, G and B channels, and then perform DBN on the R, G and B channels,

**Table 3**  
Parameters of SAE and DBN for the ADL Kidney dataset.

	SAE	DBN
Hidden node	100	100
Layer	3	2 RBMs
Batch size	400	200
Epoch	1000	600

**Table 4**  
Classification results of different feature learning algorithms on grayscale images from the HCC dataset (UNIT: %).

	ACC	SEN	SPE
SC	85.45 $\pm$ 2.30	85.11 $\pm$ 2.21	92.73 $\pm$ 1.14
DBN	82.12 $\pm$ 2.71	82.22 $\pm$ 2.75	91.12 $\pm$ 1.38
SAE	85.15 $\pm$ 2.71	84.96 $\pm$ 2.78	92.57 $\pm$ 1.36
PCANet	89.09 $\pm$ 0.68	88.79 $\pm$ 0.71	94.49 $\pm$ 0.34
GANet	<b>90.00 <math>\pm</math> 2.53</b>	<b>89.84 <math>\pm</math> 2.63</b>	<b>94.93 <math>\pm</math> 1.29</b>

respectively; (3) the SAE-RGB algorithm that perform the same pipeline as DBN-RGB; (4) the PCANet-RGB algorithm that perform the same pipeline as DBN-RGB; (5) the GANet-RGB algorithm that perform the same pipeline as DBN-RGB; and (6) the quaternion PCANet (QPCANet) algorithm [55]. It is worth noting that for the DBN-RGB, SAE-RGB, PCANet-RGB and GANet-RGB algorithms, the learned local features from each color channel image were pooled by SPP, and then all the pooled features from the R, G, and B channels were concatenated to form the final feature vector as the input to a linear SVM classifier.

For each histopathological image dataset, we randomly sampled 10,000 patches in total from the training set, which were used to train the feature representation models of the SC, JSC, SAE, DBN, PCANet- and GANet-based algorithms, respectively. Since the patch sizes of  $17 \times 17$  has shown its feasibility and effectiveness in the PCANet framework for both HCC image dataset and ADL image dataset in our previous work [11], we still selected the same patch size for all the datasets in this work. It is worth noting that only 10,000 patches were selected to train the two-stage PCA networks, but during the SPP procedure, local patches were densely sampled from the binary-to-decimal converted images to generate local histogram features for further SPP.

The leave-one-out strategy was selected to evaluate the classification performance of different algorithms on each dataset. That is to say, a single observation from the all the samples as the test set of the SVM classifier and the remaining observations as the training set. This was repeated such that each observation in all samples was used once as the test set. The cross-validation technique with grid search strategy was used to adjust the hyperparameters of SVM model. Moreover, the above experiments were repeated five times by randomly sampling patches in order to avoid the bias introduced by the patch selection. We calculated the classification accuracy, sensitivity and specificity as evaluation indices, and the results were given in the form of mean  $\pm$  SD (standard deviation). A paired-sample *t*-test was used to statistically evaluate the performance of the proposed QGANet algorithm. The results were declared statistically significant if the *p*-value was less than 0.05. Moreover, the receiver operating characteristic (ROC) curve and the value of the area under ROC curve (AUC) were also used to evaluate the algorithms for the binary-class classification task.

### 3.3. Results on HCC image dataset

Table 4 shows the classification results of GANet and other feature learning algorithms on the grayscale images from the HCC dataset. It can be seen that GANet is superior to all the

**Table 5**  
Classification results of different feature learning algorithms on color images from the HCC dataset (UNIT: %).

	ACC	SEN	SPE
JSC	87.56 $\pm$ 1.27	87.50 $\pm$ 1.25	93.76 $\pm$ 0.63
DBN-RGB	82.73 $\pm$ 1.36	82.81 $\pm$ 1.38	91.44 $\pm$ 0.68
SAE-RGB	87.27 $\pm$ 0.83	87.09 $\pm$ 0.87	93.65 $\pm$ 0.42
PCANet-RGB	85.45 $\pm$ 1.36	85.15 $\pm$ 1.56	92.66 $\pm$ 0.73
GANet-RGB	87.88 $\pm$ 1.52	87.65 $\pm$ 1.56	93.86 $\pm$ 0.77
QPCANet	88.79 $\pm$ 2.03	88.51 $\pm$ 2.06	94.34 $\pm$ 1.02
QGANet	<b>91.21 <math>\pm</math> 0.68</b>	<b>90.99 <math>\pm</math> 0.67</b>	<b>95.56 <math>\pm</math> 0.34</b>

**Table 6**  
Results of paired-samples *t*-test for the evaluation indexes of QGANet vs. other algorithms on the HCC dataset.

	ACC	SEN	SPE
SC	<0.05	<0.05	<0.05
DBN	<0.05	<0.05	<0.05
SAE	<0.05	<0.05	<0.05
PCANet	<0.05	<0.05	<0.05
GANet	<b>0.689</b>	<b>0.458</b>	<b>0.665</b>
JSC	<0.05	<0.05	<0.05
DBN-RGB	<0.05	<0.05	<0.05
SAE-RGB	<0.05	<0.05	<0.05
PCANet-RGB	<0.05	<0.05	<0.05
GANet-RGB	<0.05	<0.05	<0.05
QPCANet	<0.05	<0.05	<0.05

compared algorithms with the best mean classification accuracy of  $90.00 \pm 2.53\%$ , sensitivity of  $89.84 \pm 2.63\%$  and specificity of  $94.93 \pm 1.29\%$ . GANet has improvements of 0.91% and 1.05% over PCANet on accuracy and sensitivity, respectively, which indicates that the GA algorithm is more effective than PCA for histopathological images. Moreover, it also achieves at least 4.55%, 4.73% and 2.20% improvements on accuracy, sensitivity and specificity, respectively, compared with the SC, DBN and SAE algorithms.

Table 5 gives the results of QGANet and the compared algorithms on the color histopathological images from the HCC dataset. It is observed that QGANet outperforms all other algorithms in all evaluation indices, which achieves the classification accuracy of  $91.21 \pm 0.68\%$ , sensitivity of  $90.99 \pm 0.67\%$  and specificity of  $95.56 \pm 0.34\%$ . It is improved by 2.42%, 2.48% and 1.22% compared with the second-place performance of QPCANet. While compared with the JSC, DBN-RGB, SAE-RGB, PCANet-RGB and GANet-RGB algorithms, QGANet also achieves at least 3.33%, 3.34% and 1.70% of the corresponding improvements. Both QGANet and QPCANet are superior to the other algorithms in Table 5, indicating the effectiveness of quaternion algebra for color images.

As shown in Table 6, QGANet achieves significant improvements over all the compared algorithms on classification accuracy, sensitivity and specificity ( $p < 0.05$ ), with the only exception being GANet on the HCC dataset.

### 3.4. Results on BIDMC image dataset

Table 7 shows the classification results of GANet and other feature learning algorithms on the grayscale images from the BIDMC dataset. It can be seen that GANet is overall superior to the SC, DBN and PCANet, with the second-best mean classification accuracy of  $74.90 \pm 1.07\%$ , sensitivity of  $55.00 \pm 3.54\%$  and specificity of  $89.68 \pm 2.89\%$ . GANet improves 1.57%, 1.00% and 1.29% over PCANet on accuracy, sensitivity and specificity, respectively. As shown in Fig. 5(a) and Table 9, GANet surpasses all the compared algorithms on the AUC value (0.861) for grayscale histopathological images.

Table 8 gives the results of QGANet and the compared algorithms on the color images from the BIDMC dataset. It is ob-

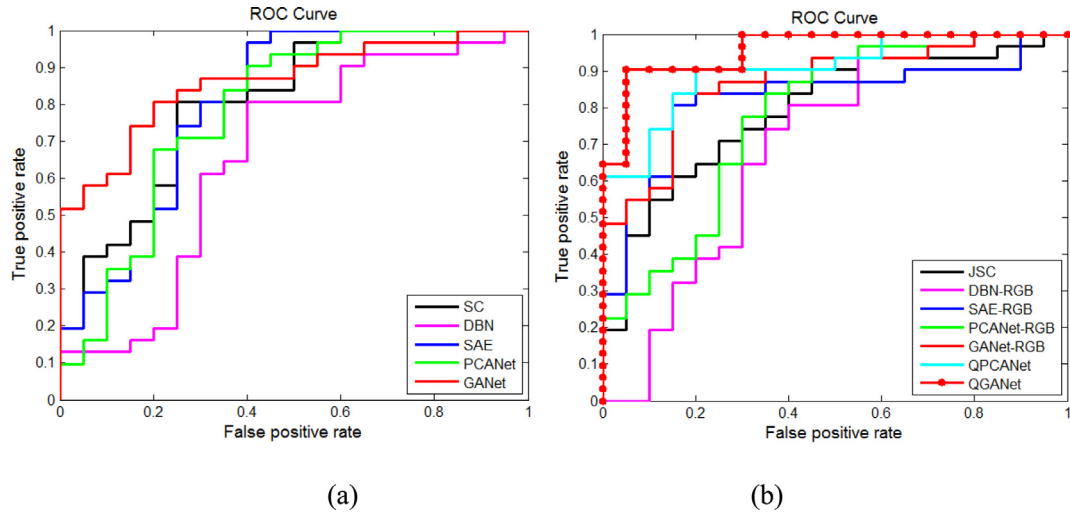


**Fig. 5.** ROC curves of different algorithms on the BIDMC dataset. (a) ROC curves of different algorithms for the grayscale histopathological images; and (b) ROC curves of different algorithms for color histopathological images.

**Table 7**

Classification results of different feature learning algorithms on grayscale images from the BIDMC dataset (UNIT: %).

	ACC	SEN	SPE
SC	72.94 ± 2.65	42.00 ± 5.70	<b>92.90 ± 2.70</b>
DBN	70.20 ± 4.25	52.00 ± 4.47	83.23 ± 1.44
SAE	<b>76.47 ± 3.10</b>	<b>63.00 ± 2.73</b>	85.16 ± 4.89
PCANet	73.33 ± 2.97	54.00 ± 4.47	88.39 ± 3.95
GANet	74.90 ± 1.07	55.00 ± 3.54	89.68 ± 2.89

**Table 8**

Classification results of different feature learning algorithms on color images from the BIDMC dataset (UNIT: %).

	ACC	SEN	SPE
JSC	74.51 ± 2.77	46.00 ± 5.48	92.90 ± 1.44
DBN-RGB	71.37 ± 1.07	44.00 ± 7.42	89.03 ± 4.33
SAE-RGB	78.43 ± 2.15	<b>70.00 ± 6.32</b>	83.87 ± 2.04
PCANet-RGB	78.04 ± 2.56	53.00 ± 5.70	94.19 ± 1.44
GANet-RGB	75.69 ± 3.28	53.00 ± 7.58	90.32 ± 2.28
QPCANet	81.96 ± 0.88	66.00 ± 2.24	92.26 ± 1.77
QGANet	<b>85.49 ± 1.07</b>	66.25 ± 2.50	<b>97.58 ± 1.61</b>

served that QGANet outperforms all the compared algorithms on classification accuracy and specificity, which are  $85.49 \pm 1.07\%$  and  $97.58 \pm 1.61\%$ , respectively. Moreover, it achieves improvements of 3.53%, 0.25% and 5.32% on accuracy, sensitivity and specificity, respectively, compared with the second place performance of QPCANet. When compared with all the other non-quaternion-based algorithms, QGANet results in at least 7.06% and 3.39% improvements on accuracy and specificity, respectively. Moreover, QGANet outperforms all compared algorithms on AUC value (0.958), as shown in Fig. 5(b) and Table 9.

Again, as can be seen from Table 10, QGANet achieves significant improvements over all the compared algorithms on both classification accuracy and specificity ( $p < 0.05$ ), and it is also significantly superior to all other algorithms on sensitivity ( $p < 0.05$ ) except SAE-RGB and QPCANet.

### 3.5. Results on ADL kidney image dataset

Table 11 gives the classification results of GANet and other algorithms on the grayscale images from the ADL kidney image dataset. GANet achieves the best specificity of  $83.20 \pm 3.03\%$ , and

**Table 9**

The AUC values of different algorithms on the BIDMC dataset.

Grayscale Images	AUC	Color Images	AUC
SC	0.805	JSC	0.794
DBN	0.660	DBN-RGB	0.705
SAE	0.803	SAE-RGB	0.826
PCANet	0.784	PCANet-RGB	0.776
GANet	<b>0.861</b>	GANet-RGB	0.873
/	/	QPCANet	0.905
/	/	QGANet	<b>0.958</b>

**Table 10**

Results of paired-samples *t*-Test for the evaluation indexes Of QGANet vs. other algorithms on the BIDMC dataset.

	ACC	SEN	SPE
SC	<0.05	<0.05	<0.05
DBN	<0.05	<0.05	<0.05
SAE	<0.05	<0.05	<0.05
PCANet	<0.05	<0.05	<0.05
GANet	<0.05	<0.05	<0.05
JSC	<0.05	<0.05	<0.05
DBN-RGB	<0.05	<0.05	<0.05
SAE-RGB	<0.05	<b>0.402</b>	<0.05
PCANet-RGB	<0.05	<0.05	<0.05
GANet-RGB	<0.05	<0.05	<0.05
QPCANet	<0.05	<b>0.545</b>	<0.05

**Table 11**

Classification results of different feature learning algorithms on grayscale images from the ADL Kidney dataset (UNIT: %).

	ACC	SEN	SPE
SC	79.80 ± 2.59	78.00 ± 1.41	81.60 ± 3.84
DBN	77.60 ± 1.34	72.40 ± 2.19	82.80 ± 1.09
SAE	<b>82.40 ± 1.52</b>	<b>86.40 ± 0.89</b>	78.40 ± 2.19
PCANet	<b>82.40 ± 1.95</b>	84.80 ± 2.28	80.00 ± 2.45
GANet	81.80 ± 0.84	80.40 ± 2.60	<b>83.20 ± 3.03</b>

the second place of accuracy ( $81.80 \pm 0.84\%$ ). It is also superior to other compared algorithms with the best AUC value (0.910) in Table 13 with the ROC curves in Fig. 6(a).

Table 12 shows the results of QGANet and the compared algorithms on the color images from the ADL kidney image dataset.

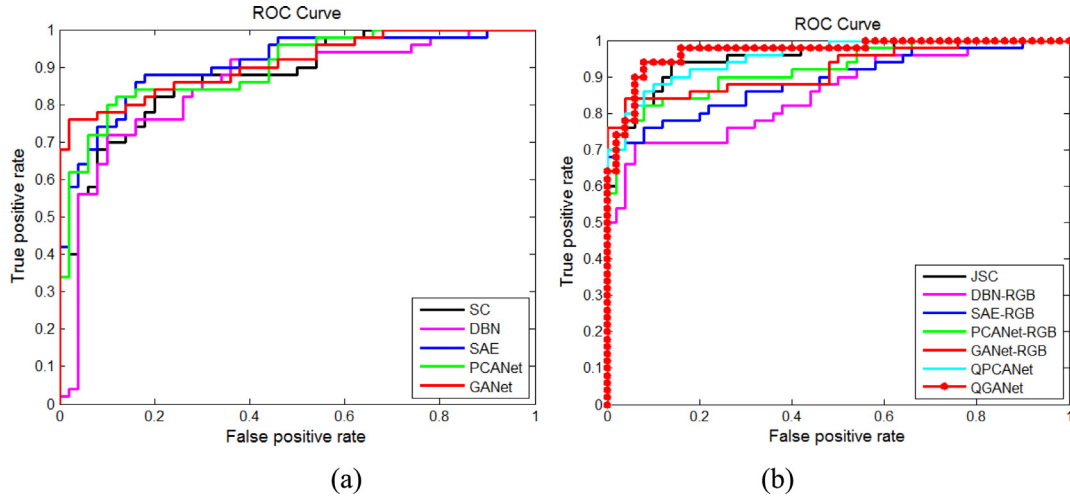


**Fig. 6.** ROC curves of different algorithms on the ADL Kidney dataset. (a) ROC curves of different algorithms for the grayscale histopathological images; and (b) ROC curves of different algorithms for the color histopathological images.

**Table 12**

Classification results of different feature learning algorithms on color images from the ADL Kidney dataset (UNIT: %).

	ACC	SEN	SPE
JSC	$87.20 \pm 0.84$	$89.60 \pm 0.89$	$84.80 \pm 1.10$
DBN-RGB	$80.60 \pm 1.67$	$92.40 \pm 2.61$	$68.80 \pm 1.79$
SAE-RGB	$86.20 \pm 1.30$	<b><math>94.80 \pm 3.03</math></b>	$72.40 \pm 1.67$
PCANet-RGB	$84.40 \pm 1.14$	$86.80 \pm 1.10$	$82.00 \pm 1.41$
GANet-RGB	$85.80 \pm 1.92$	$88.80 \pm 3.03$	$82.80 \pm 1.10$
QPCANet	$88.40 \pm 0.55$	$93.20 \pm 1.10$	$83.60 \pm 1.67$
QGANet	<b><math>90.20 \pm 1.31</math></b>	$93.60 \pm 0.89$	<b><math>86.80 \pm 1.79</math></b>

**Table 13**

The AUC values of different algorithms on the ADL Kidney dataset.

Grayscale images	AUC	Color images	AUC
SC	0.877	JSC	0.952
DBN	0.851	DBN-RGB	0.855
SAE	0.908	SAE-RGB	0.891
PCANet	0.898	PCANet-RGB	0.922
GANet	<b>0.910</b>	GANet-RGB	0.922
/	/	QPCANet	0.955
/	/	QGANet	<b>0.968</b>

It can be found that QGANet achieves the best classification accuracy of  $90.20 \pm 1.31\%$  and specificity of  $86.80 \pm 1.79\%$ , as well as the second-best sensitivity of  $93.60 \pm 0.89\%$ . QGANet has improvements of 1.80% and 3.20% over QPCANet on accuracy and specificity, respectively. Moreover, QGANet makes improvements of at least 3.00% and 2.00% on the classification accuracy and specificity, respectively, compared with the JSC, DBN-RGB, SAE-RGB, PCANet-RGB and GANet-RGB. Moreover, as shown in Fig. 6(b) and Table 13, QGANet outperforms all compared algorithms on AUC value (0.968).

As shown in Table 14, QGANet achieves significant improvements over all the compared algorithms on classification accuracy ( $p < 0.05$ ); it also significantly surpasses all other algorithms on sensitivity ( $p < 0.05$ ) except for DBN-RGB, SAE-RGB and QPCANet, and it significantly outperforms all the other compared algorithms on specificity ( $p < 0.05$ ) except for GANet and PCANet-RGB.

**Table 14**

Results of paired-samples  $t$ -test for the evaluation indexes of QGANet vs. other algorithms on the ADL Kidney dataset.

	ACC	SEN	SPE
SC	<0.05	<0.05	<0.05
DBN	<0.05	<0.05	<0.05
SAE	<0.05	<0.05	<0.05
PCANet	<0.05	<0.05	<0.05
GANet	<0.05	<0.05	<b>0.052</b>
JSC	<0.05	<0.05	<0.05
DBN-RGB	<0.05	<b>0.359</b>	<0.05
SAE-RGB	<0.05	<b>0.421</b>	<0.05
PCANet-RGB	<0.05	<0.05	<b>0.371</b>
GANet-RGB	<0.05	<0.05	<0.05
QPCANet	<0.05	<b>0.545</b>	<0.05

#### 4. Discussion

PCANet is a novel DL algorithm with much simpler network architecture and parameters. In this work, we first propose a GANet algorithm motivated by PCANet. As shown in the experiments, GANet can achieve even superior performance over PCANet on the HCC dataset and the BIDMC dataset, and it can also obtain competitive results as compared to PCANet on the ADL Kidney dataset. The experimental results indicate that GANet is more robust and effective than PCANet in the feature representation of grayscale histopathological images, since GA is operated on the Grassmann manifold to well represent the intrinsic data manifold. In addition, GA is expected to be more robust to outliers than PCA from the viewpoint of energy minimization [46].

The color information is critical for the diagnosis of histopathological images. Owing to lack of mechanism of fusing or representing color information, GANet, however, cannot well represent color images. Since quaternion algebra can well handle color images, Therefore, a novel quaternion GANet (QGANet), based on our proposed QGA algorithm, is then developed. It integrates quaternion algebra, which is good at handling color images, with GA. The proposed QGANet can effectively fuse colors by decomposing and representing a color image into the one real and three imaginary parts with quaternion algebra. Therefore, QGANet learns superior feature representation for color histopathological images, which outperforms all the compared algorithms on all the three datasets.



It is worth noting that the results of the DBN and SAE are unsatisfactory in the current work. One possible reason is that the training samples are not large enough for both DBN and SAE, since we only randomly select 10,000 patches as the training set for all algorithms for a fair comparison in this study. More training samples, more computational effort required for the DL algorithms. This indicates that QGANet can still achieve excellent performance with a non-large-scale training dataset of histopathological images. On the other hand, both the DBN and SAE are used as the unsupervised learning algorithms without fine-tuning in this work, which further degrades their performance.

Although QGANet has shown its effectiveness of feature representation for histopathological images, it has high computational complexity. The original GA algorithm itself requires number of iterations in calculation, resulting in higher computational complexity than PCANet. After the quaternion algebra is embedded to GA algorithm, the computational complexity of QGANet is 4 times of that of GANet. In future work, we will optimize the proposed QGANet algorithm with GPU to improve the running time.

In the current work, we mainly study the effectiveness of the proposed QGANet algorithm by comparing it with other algorithms. In our future work, a comprehensive ablation study will be performed with different settings (e.g. patch sizes, layers, filters, and so on) to further evaluate the robustness of QGANet algorithm. The current variants of PCANet mainly focus on using more effective filters instead of PCA to improve the representation performance. In fact, the method of binary hashing in PCANet also affects the representation performance [9], which has not been deeply investigated yet. In future work, different binary encoding methods will be studied in QGANet to further improve the performance. We will also study the feasibility of combining the unsupervised QGANet with the supervised CNN to further improve the classification performance, while in which the QGANet does not need the block-wise histograms model anymore. Moreover, the final feature vector is the concatenation of all SPP features from different PC images, which has very high feature dimensionality to result in the curse of dimensionality. Therefore, we can take each of the output four-channel quaternion images as a single view, and then apply the multi-view CNN algorithm to effectively fuse the four-channel quaternion images that are generated by the cascaded QGA module to improve the final feature representation.

## 5. Conclusions

In conclusion, we first propose a GANet algorithm as an alternative unsupervised representation learning algorithm for images motivated by the PCANet framework, and then apply it to grayscale histopathological image analysis. Secondly, a QGA algorithm is developed by integrating quaternion algebra with GA. It can effectively retain and fuse color information in color histopathological images. Lastly, the QGANet algorithm, with high performance on feature representation of color histopathological images, is proposed. The experimental results on three histopathological image datasets have demonstrated the effectiveness of the proposed QGANet algorithm, indicating its great potential in the area of digital pathology.

In future work, a more comprehensive ablation study should be conducted to further evaluate the proposed QGANet algorithm. The optimization algorithm for QGANet will also be studied to overcome its high computational complexity. Moreover, we will investigate the combination of QGANet with recently advanced deep learning frameworks to further improve its performance for color histopathological image based CAD.

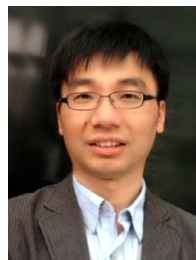
## Acknowledgements

This work is supported by the National Natural Science Foundation of China (61471231, 81627804, 61671281, 11471208), and the Shanghai Science and Technology Foundation (17411953400, 18010500600), Shanghai Hospital Development Center (16CR3061B).

## References

- [1] M. Gurcan, L. Boucheron, A. Can, A. Madabhushi, N. Rajpoot, B. Yener, Histopathological image analysis: a review, *IEEE Rev. Biomed. Eng.* 2 (2009) 147–171.
- [2] H. Irshad, A. Veillard, L. Roux, D. Racoceanu, Methods for nuclei detection, segmentation and classification in digital histopathology: a review – current status and future potential, *IEEE Rev. Biomed. Eng.* 7 (2014) 97–114.
- [3] C. Zhong, J. Han, A. Borowsky, B. Parvin, Y. Wang, H. Chang, When machine vision meets histology: a comparative evaluation of model architecture for classification of histology sections, *Med. Image Anal.* 35 (2017) 530–543.
- [4] M. Veta, J.W. Pluim, P. Diest, M. Viergever, Breast cancer histopathology image analysis: a review, *IEEE Trans. Biomed. Eng.* 61 (5) (2014) 1400–1411.
- [5] C. Lopez, S. Agaian, A. Hoyos, I. Thompson, Computer-aided prostate cancer diagnosis from digitized histopathology: a review on texture-based systems, *IEEE Rev. Biomed. Eng.* 8 (2015) 98–113.
- [6] F. Xing, L. Yang, Robust nucleus/cell detection and segmentation for digital pathology and microscopic images: a comprehensive review, *IEEE Rev. Biomed. Eng.* 9 (2016) 234–263.
- [7] G. Litjens, C. Sanchez, N. Timofeeva, M. Hermesen, I. Nagtegaal, I. Kovacs, C. Kaa, P. Bult, B. Ginneken, J. Laak, Deep learning as a tool for increased accuracy and efficiency of histopathological diagnosis, *Sci. Rep.* 6 (2016) 26286.
- [8] J. Arevalo, A. Roa, V. Arias, E. Romero, F. Gonzalez, An unsupervised feature learning framework for basal cell carcinoma image analysis, *Artif. Intell. Med.* 64 (2) (2015) 131–145.
- [9] L. He, L.R. Long, S. Antani, G.R. Thoma, Histology image analysis for carcinoma detection and grading, *Comput. Methods Programs Biomed.* 107 (3) (2012) 538–556.
- [10] C. Lu, M. Mandal, Automated analysis and diagnosis of skin melanoma on whole slide histopathological images, *Pattern Recognit.* 48 (2015) 2738–2750.
- [11] J. Shi, J. Wu, Y. Li, Q. Zhang, S. Ying, Histopathological image classification with color pattern random binary hashing based PCANet and matrix-form classifier, *IEEE J. Biomed. Health Inform.* 21 (5) (2017) 1327–1337.
- [12] A. Janowczyk, A. Madabhushi, Deep learning for digital pathology image analysis: a comprehensive tutorial with selected use cases, *J. Pathol. Inform.* 7 (1) (2016) 29.
- [13] Y. Bengio, A. Courville, P. Vincent, Representation learning: a review and new perspectives, *IEEE Trans. Pattern Anal. Mach. Intell.* 35 (8) (2013) 1798–1828.
- [14] Y. LeCun, Y. Bengio, G. Hinton, Deep learning, *Nature* 521 (7553) (2015) 436–444.
- [15] H. Qiao, Y. Li, F. Li, X. Fu, X. Yang, W. Wu, Biologically inspired model for visual cognition achieving unsupervised episodic and semantic feature learning, *IEEE Trans. Cybern.* 46 (10) (2016) 2335–2347.
- [16] D. Ciresan, A. Giusti, L. Gambardella, J. Schmidhuber, in: *Mitosis Detection in Breast Cancer Histology Images With Deep Neural Networks*, MICCAI, 2013, pp. 411–418.
- [17] Y. Xie, F. Xing, X. Kong, H. Su, L. Yang, in: *Beyond classification: Structured Regression For Robust Cell Detection Using Convolutional Neural Network*, MICCAI, 2015, pp. 358–365.
- [18] Y. Xu, Z. Jia, Y. Ai, F. Zhang, M. Lai, E. Chang, in: *Deep Convolutional Activation Features For Large Scale Brain Tumor Histopathology Image Classification and Segmentation*, ICASSP, 2015, pp. 947–951.
- [19] F. Liu, L. Yang, in: *A Novel Cell Detection Method Using Deep Convolutional Neural Network and Maximum-Weight Independent Set*, MICCAI, 2015, pp. 349–357.
- [20] K. Sirinukunwattana, S. Raza, Y. Tsang, D. Snead, I. Cree, N. Rajpoot, Locality sensitive deep learning for detection and classification of nuclei in routine colon cancer histology images, *IEEE Trans. Med. Imag.* 35 (5) (2016) 1196–1206.
- [21] J. Xu, X. Luo, G. Wang, H. Gilmore, A. Madabhushi, A deep convolutional neural network for segmenting and classifying epithelial and stromal regions in histopathological images, *Neurocomputing* 191 (2016) 214–223.
- [22] Z. Xu, J. Huang, in: *Detecting 10000 Cells in One Second*, MICCAI, 2016, pp. 676–684.
- [23] S. Wang, J. Yao, Z. Xu, J. Huang, in: *Subtype Cell Detection With an Accelerated Deep Convolution Neural Network*, MICCAI, 2016, pp. 640–648.
- [24] Y. Xu, Y. Li, M. Liu, Y. Wang, M. Lai, E. Chang, in: *Gland Instance Segmentation By Deep Multi Channel Side Supervision*, MICCAI, 2016, pp. 496–504.
- [25] H. Chen, Q. Dou, X. Wang, J. Qin, P. Heng, in: *Mitosis Detection in Breast Cancer Histology Images Via Deep Cascaded Networks*, AAAI, 2016, pp. 1160–1166.
- [26] T. Wan, J. Cao, J. Chen, Z. Qin, Automated grading of breast cancer histopathology using cascaded ensemble with combination of multi-level image features, *Neurocomputing* 229 (2017) 34–44.
- [27] Y. Xu, Z. Jia, L.B. Wang, Y. Ai, F. Zhang, M. Lai, E.I.C. Chang, Large scale tissue histopathology image classification, segmentation, and visualization via deep convolutional activation features, *BMC Bioinf.* 18 (2017) 281.

- [28] N. Kumar, R. Verma, S. Sharma, S. Bhargava, A. Vahadane, A. Sethi, A dataset and a technique for generalized nuclear segmentation for computational pathology, *IEEE Trans. Med. Imag.* 36 (7) (2017) 1550–1560.
- [29] Y. Xie, F. Xing, X. Shi, X. Kong, H. Su, L. Yang, Efficient and robust cell detection: a structured regression approach, *Med. Image Anal.* (2017).
- [30] Y. Zheng, Z. Jiang, F. Xie, H. Zhang, Y. Ma, H. Shi, Y. Zhao, Feature extraction from histopathological images based on nucleus-guided convolutional neural network for breast lesion classification, *Pattern Recognit.* 71 (2017) 14–25.
- [31] Z. Zhang, P. Chen, M. Sapkota, L. Yang, in: TandemNet: Distilling Knowledge from Medical Images Using Diagnostic Reports As Optional Semantic References, *MICCAI*, 2017, pp. 320–328.
- [32] Z. Zhang, Y. Xie, F. Xing, M. McGough, L. Yang, in: MDNet: a Semantically and Visually Interpretable Medical Image Diagnosis Network, *CVPR*, 2017, pp. 3549–3557.
- [33] A. Roa, J. Ovalle, A. Madabhushi, F. Gonzalez, in: A Deep Learning Architecture For Image representation, Visual Interpretability and Automated Basal-Cell Carcinoma Cancer Detection, *MICCAI*, 2013, pp. 403–410.
- [34] N. Nayak, H. Chang, A. Borowsky, P. Spellman, B. Parvin, in: Classification of Tumor Histopathology Via Sparse Feature Learning, *ISBM*, 2013, pp. 410–413.
- [35] P. Maqin, R. Thamburaj, J. Mammen, M. Manipadam, in: Automated Nuclear Pleomorphism Scoring in Breast Cancer Histopathology Images Using Deep Neural Networks, *MIKE*, 2015, pp. 269–276.
- [36] J. Xu, L. Xiang, Q. Liu, H. Gilmore, J. Wu, J. Tang, A. Madabhushi, Stacked sparse autoencoder (SSAE) for nuclei detection on breast cancer histopathology images, *IEEE Trans. Med. Imag.* 35 (1) (2016) 119–130.
- [37] X. Zhang, H. Dou, T. Ju, J. Xu, S. Zhang, Fusing heterogeneous features from stacked sparse autoencoder for histopathological image analysis, *IEEE J. Biomed. Health Inform.* 20 (5) (2016) 1377.
- [38] T. Chan, K. Jia, S. Gao, J. Lu, Z. Zeng, Y. Ma, PCANet: a simple deep learning baseline for image classification, *IEEE Trans. Image Process.* 24 (12) (2015) 5017–5032.
- [39] Z. Feng, L. Jin, D. Tao, S. Huang, DLNet: a manifold-learning-based discriminative feature learning network for scene classification, *Neurocomputing* 157 (2015) 11–21.
- [40] L. Tian, C. Fan, Y. Ming, J. Shi, in: SRDNet: an Efficient Deep Learning Algorithm For Face Analysis, *ICIRA*, 2015, pp. 499–510.
- [41] L. Tian, C.X. Fan, Y. Ming, Y. Jin, in: Stacked PCA Network (SPCANet): an Effective Deep Learning For Face Recognition, *DSP*, 2015, pp. 1039–1043.
- [42] D. Yu, X.J. Wu, 2DPCANet: a deep leaning network for face recognition, *Multimed. Tools Appl.* (2017) 1–16.
- [43] J. Wu, S. Qiu, R. Zeng, Y. Kong, L. Senhadji, H. Shu, Multilinear principal component analysis network for tensor object classification, *IEEE Access* 5 (2017) 3322–3331.
- [44] B. Pan, Z. Shi, X. Xu, R-VCANet: a new deep-learning-based hyperspectral image classification method, *IEEE J. Sel. Topics Appl. Earth Observ.* 10 (5) (2017) 1975–1986.
- [45] F. Nie, J. Yuan, H. Huang, in: Optimal Mean Robust Principal Component Analysis, *ICML*, 2014, pp. 1062–1070.
- [46] S. Hauberg, A. Feragen, M. Black, in: Grassmann Averages For Scalable Robust PCA, in *Proc. CVPR*, 2014, pp. 3810–3817.
- [47] L. Li, S. Liu, Y. Peng, Z. Sun, Overview of principal component analysis algorithm, *Opt.-Int. J. Light Electron Opt.* 127 (9) (2016) 3935–3944.
- [48] W. Hamilton, Elements of quaternions, *Nature* 60 (1556) (1899) 387.
- [49] L. Guo, M. Dai, M. Zhu, Quaternion moment and its invariants for color object classification, *Inform. Sci.* 273 (2014) 132–143.
- [50] H. Li, Z. Liu, Y. Huang, Y. Shi, Quaternion generic Fourier descriptor for color object recognition, *Pattern Recognit.* 48 (12) (2015) 3895–3903.
- [51] Y. Xu, L. Yu, H. Xu, H. Zhang, T. Nguyen, Vector sparse representation of color image using quaternion matrix analysis, *IEEE Trans. Image Process.* 24 (4) (2015) 1315–1329.
- [52] V. Risojevic, Z. Babic, Unsupervised quaternion feature learning for remote sensing image classification, *IEEE J. Sel. Topics Appl. Earth Observ.* 9 (4) (2016) 1521–1531.
- [53] R. Lan, Y. Zhou, Y. Tang, Quaternionic local ranking binary pattern: a local descriptor of color images, *IEEE Trans. Image Process.* 25 (2) (2016) 566–579.
- [54] N. Le Bihan, S.J. Sangwine, in: Quaternion Principal Component Analysis of Color Images, *ICIP*, 2003, pp. 809–812.
- [55] R. Zeng, J. Wu, Z. Shao, Color image classification via quaternion principal component analysis network, *Neurocomputing* 216 (2016) 416–428.
- [56] J. Wu, J. Shi, S. Ying, Q. Zhang, Y. Li, in: Learning Representation For Histopathological Image With Quaternion Grassmann average Network, *MICCAI Workshop MLMI*, 2016, pp. 122–129.
- [57] S. Lazebnik, C. Schmid, J. Ponce, in: Beyond Bags of features: Spatial Pyramid Matching For Recognizing Natural Scene Categories, *CVPR*, 2006, pp. 2169–2178.
- [58] V. Vapnik, *Statistical Learning Theory*, John Wiley & Sons, New York, 1998.
- [59] J. Shi, Y. Li, J. Zhu, H. Sun, Y. Cai, Joint sparse coding based spatial pyramid matching for classification of color medical image, *Comput. Med. Imag. Graph.* 41 (1) (2015) 61–66.
- [60] F. Dong, H. Irshad, E. Oh, M. Lerwill, E. Brachtel, N. Jones, N. Knoblauch, L. Kouhsari, N. Johnson, L. Rao, B. Jones, D. Wibue, S. Schnitt, A. Beck, Computational pathology to discriminate benign from malignant intraductal proliferations of the breast, *PLoS One* 9 (12) (2014) e0114885.
- [61] U. Srinivas, H. Mousavi, C. Jeon, V. Monga, A. Hattel, B. Jayarao, in: SHIRC: a Simultaneous Sparsity Model For Histopathological Image Representation and Classification, *ISBI*, 2013, pp. 1106–1109.
- [62] J. Yang, K. Yu, Y. Gong, T. Huang, in: Linear Spatial Pyramid Matching Using Sparse Coding For Image Classification, *CVPR*, 2009, pp. 1794–1801.
- [63] G. Hinton, S. Osindero, Y. Teh, A fast learning algorithm for deep belief nets, *Neural Comput.* 18 (7) (2016) 1527–1554.
- [64] Y. Bengio, P. Lamblin, D. Popovici, H. Larochelle, in: Greedy Layerwise Training of Deep Networks, *NIPS*, 2006, pp. 153–160.



**Jun Shi** received the B.S. degree and the Ph.D. degree from the Department of Electronic Engineering and Information Science, University of Science and Technology of China in 2000 and 2005, respectively. In 2005, he joined the School of Communication and Information Engineering, Shanghai University, China, where he has been a Professor since 2015. From 2011 to 2012, he was a visiting scholar with the University of North Carolina at Chapel Hill. His current research interests include machine learning in medical imaging.



**Xiao Zheng** received the B.S. degree of biomedical engineering from Wenzhou Medical University in 2015. She is a M.Sc. candidate in the School of Communication and Information Engineering, Shanghai University, China now. Her research interests include the machine learning for medical images.



**Jinjie Wu** received the B.S. degree from the School of Electrical and Information Engineering, Jiangsu University in 2013. He is a M.Sc. candidate in the School of Communication and Information Engineering, Shanghai University, China now. His research interests include the machine learning for medical images.



**Qi Zhang** received his B.S. degree in Electronic Engineering in 2005 and Ph.D. degree in Biomedical Engineering in 2010, both from Fudan University, China. From 2008 to 2009, he was a visiting Ph.D. student at the Department of Biomedical Engineering, Duke University, USA. He joined the Institute of Biomedical Engineering, Shanghai University, China in 2010, and then was an Associate Professor since 2013. His research interests include medical signal processing, biomedical modeling and computer aided diagnosis.



**Shihui Ying** received his B.Eng. degree in Mechanical Engineering and Ph.D. degree in Applied Mathematics from Xi'an Jiaotong University, Xi'an, China in July 2001 and April 2008, respectively. He is currently a professor with the Department of Mathematics, School of Science, Shanghai University, Shanghai, China. He was a postdoctor in Biomedical Research Imaging Center (BRIC), University of North Carolina at Chapel Hill, U.S.A., from 2012 to 2013. He is also a member of IEEE from 2009 and services as an Editor of JSM Mathematics and Statistics from Jan, 2013. His research interests cover mathematical theory and methods for machine learning and medical image analysis.